

Scanning Tunnelling Microscopy and Transport Spectroscopy at low temperatures

Jithin Bhagavathi

*A dissertation submitted for the partial fulfilment
of a BS-MS dual degree in Science*



**Indian Institute of Science Education and Research Mohali
April 2014**

Certificate of Examination

This is to certify that the dissertation titled **Scanning Tunnelling Microscopy and Transport Spectroscopy at low temperatures** submitted by **Jithin Bhagavathi** (Reg. No. MS09064) for the partial fulfillment of BS-MS dual degree programme of the Institute, has been examined by the thesis committee duly appointed by the Institute. The committee finds the work done by the candidate satisfactory and recommends that the report be accepted.

Dr. Sanjeev Kumar

Dr. Yogesh Singh

Dr. Goutam Sheet
(Supervisor)

Dated: April 25, 2014

Declaration

The work presented in this dissertation has been carried out by me under the guidance of Dr. Goutam Sheet at the Indian Institute of Science Education and Research Mohali.

This work has not been submitted in part or in full for a degree, a diploma, or a fellowship to any other university or institute. Every effort has been made to acknowledge contributions of fellow researchers wherever applicable. This thesis is a bonafide record of original work done by me and all sources listed within have been detailed in the bibliography.

Jithin Bhagavathi
(Candidate)

Dated: April 25, 2014

In my capacity as the supervisor of the candidate's project work, I certify that the above statements by the candidate are true to the best of my knowledge.

Dr. Goutam Sheet
(Supervisor)

Acknowledgments

There are several people I have to thank for having made the past year an enjoyable experience.

First, I must thank my advisor, Dr. Goutam Sheet, for all his guidance, encouragement, and patience over the course of my work in his lab. I am indeed fortunate to have had the opportunity to use a variety of sophisticated instruments at the lab, and am grateful to him for introducing me to very interesting avenues of research, and providing me with the right resources.

I am indebted to Kenneth Kollin from RHK technologies for all the timely assistance I received from him while building the scanning Tunnelling Microscope. His accurate troubleshooting skills have saved me a lot of trouble.

My gratitude is extended to Mr. Subash Pai for the help I received for the Point Contact Spectroscopy probe, and I would like to declare the important contribution of Mr. Sikandar Singh in expertly taking care of a large variety of custom machining jobs that were required as part of my work.

A lot of my work would not have been possible without the use of Dr Yogesh Singh's Laboratory, and I am grateful for his support and faith. I cannot thank Ashwini Balodhi enough for lending his expertise in using the PPMS cryostat as often as I required it.

Thanks to Ashima, Avtar, Jagmeet and Leena for making the lab a fun place to be in. Their assistance and cooperation have helped me a lot. Thanks to Abhishek for chipping in.

And most importantly, I would like to thank contributors to Open-Source, in particular the teams at PyQtGraph, PySide, Linux-Gpib, and Python for making my job far easier, and the results far more impressive.

Abstract

Scanning tunneling microscopes(STM) are instruments capable of extremely high spatial resolution down to sub-angstrom length scales. Their capabilities range from imaging lattice structures, to observing standing wave patterns of surface state electrons in metals, and spatial manipulation of individual atoms. Plainly speaking, they let us 'see' atoms, move them around, and more . Additional capabilities such as spin polarized tunneling microscopy have also been developed for STMs. A prerequisite for high resolution imaging, is an atomically sharp probing tip, preferably with a p_z or d_z^2 orbital at the apex. However, from the position-momentum uncertainty($\Delta x \cdot \Delta k_x \geq \frac{\hbar}{2\pi}$), it can be inferred that such a small value for Δx will result in a large error in momentum information(Δk) .

Point Contact Spectroscopy is a technique to measure the Fermi surface properties in solids by fabricating nano-metre sized 'ballistic' contacts between conductors, and measuring the current-voltage characteristics. In keeping with the position-momentum uncertainty, the large size of the contacts makes it a very powerful spectroscopic tool that is used to extract momentum and energy resolved spectroscopic information. The IV spectra is used to reveal information regarding the excitation energies of phonons, magnons, quasi-particles in superconductors etc. This technique when applied to nano-constrictions formed between metals and superconductors, can be used to extract the magnitude and momentum space symmetry of the superconducting energy gap by fitting with theoretical formalisms, and this is known as Point Contact Andreev Reflection(PCAR) Spectroscopy.

During the course of this thesis, I have developed two major instruments for investigating the physical properties of solids down nano-metre length scales at low-temperatures and high magnetic fields.

1) A scanning tunneling microscope was developed and calibrated. It was also used to image atomic steps in Highly Oriented Pyrolytic Graphite(HOPG), as well as obtain I-V spectra.

2) A low temperature probe for carrying out point contact spectroscopy was also developed in-house, and used with a liquid helium cryostat. Experiments were carried out to study the temperature and magnetic field dependence of $FeTe_{0.6}Se_{0.4}$ -Silver point contacts. Andreev reflection spectroscopy was also carried out in Niobium-Gold point contacts.

Contents

Abstract	9
List of Figures	14
1 Scanning Tunnelling Microscopy	1
1.1 Review of Scanning Tunnelling Microscopes	1
1.1.1 Electron tunnelling	2
1.1.2 Piezoceramic based fine approach and scanning	3
1.1.3 Constant current operation	4
1.1.4 Constant height operation	5
1.2 Development of a room temperature STM	6
1.2.1 Hardware	6
1.2.2 Approach procedures	8
1.3 Software	8
1.3.1 Calibration of scan ranges using a standard sample	9
1.3.2 Measurements on <i>Highly Oriented Pyrolytic Graphite</i>	12
1.3.3 Scanning tunneling spectroscopy	12
1.4 Designing a low-temperature STM	14
2 Point Contact Andreev Reflection Spectroscopy	15
2.1 Electronic transport across nano-constrictions	15
2.1.1 Thermal regime	16
2.1.2 Ballistic regime	16
2.1.3 Interpolation of Sharvin and Maxwell Regime	17
2.1.4 Critical current in nano-constrictions	17
2.1.5 Blonder, Tinkham, Klapwijk formalism for Andreev reflection in Normal metal - superconductor nano-junctions	17
2.2 Differential conductance	19
2.2.1 Measurement with a Pulsed Differential resistance setup	20
2.2.2 Measurements with a Pulsed Delta setup	21

2.3	Construction of a point contact spectroscopy probe	21
2.3.1	Mechanical structure	22
2.3.2	Wiring and electronics	22
2.3.3	Data acquisition software	24
2.3.4	Acquiring differential resistance data	26
2.3.5	Acquiring pulsed I-V data	26
2.3.6	Monitoring temperature	26
2.3.7	Stepper motor controller	27
2.4	Results and discussions	27
2.4.1	Critical current peaks in $FeTe_{0.60}Se_{0.40}$ - Silver point contacts . . .	27
2.4.2	Andreev reflection spectroscopy in Niobium-Gold contacts	30

List of Figures

1.1	Schematic diagram of the electronic wave-function as it tunnels through a physical barrier. The sample's Fermi level has been modified by applying an external bias.	2
1.2	Scan-tube with axially segmented electrodes. Potential difference applied to the electrodes causes the relevant sections to expand, and this is used to flex or expand the whole tube.	3
1.3	Flowchart indicating the control and data flow between various components of the STM	5
1.4	Various parts of the room-temperature STM's hardware.	6
1.5	Top) Waveform applied to the scan tube during coarse approach. Bottom) tunneling current signals indicating the stepping noise generated by the coarse approach motor, and the induced current from the scanning voltage.	9
1.6	Technical drawing of the calibration grating used (Courtesy : Asylum Research) ("3D Calibration Reference"). Key features are a lateral pitch of $10\mu m \pm 0.04\mu m$ and depth of $200nm \pm 4nm$	10
1.7	Topographic image of a calibration grating obtained using the STM . Inset: High-res scan of a single pit, with a line depicting the route over which depth information was extracted and has been plotted.	10
1.8	Depth profile of a single pit on the calibration grating. A depth of $\sim 700nm$, and a width of $\sim 5\mu m$ can be seen.	11
1.9	a $100nm \times 100nm$ scan on HOPG showing atomic layers.	12
1.10	a $100nm \times 100nm$ scan on HOPG showing layer boundaries.	13
1.11	I-V spectroscopy on HOPG.	13
1.12	Exploded view of the STM section of the cryostat insert designed using Solidworks.	14
2.1	Transmission and reflectance probabilities plotted for transport across an N-S junction with the energy gap of $S(\Delta) = 2meV$, and different values of the barrier potential(0,0.2,0.6,4.8).	18

2.2	Four probe connections made to a sample for measurements with a Physical Property Measurement System	20
2.3	a) The current pulses applied during pulsed differential resistance measurements b) Detailed view of the acquisition technique. Source: 2610, White paper on differential conductance measurements	21
2.4	The probe mounted on a PPMS cryostat, and connected the acquisition instruments. The additional length of the probe was provided in order to make it compatible with a deeper cryostat.	23
2.5	The cold end of the probe. A) Brass holder containing the 100t.p.i. screw. B) Delrin extender for mounting the tip holder. C) Stainless steel mounting posts D) Hypodermic needle based tip-holder fixed using Stycast epoxy adhesive E) Sample holder machined in Copper.	23
2.6	Schematic representation of the data acquisition setup	25
2.7	Screenshot of open-source software developed to interface with all the instruments.	25
2.8	Sample temperature rising by about 10mK when measurement current was swept from -15mA to 15mA in differential conductance mode	27
2.9	Experimental data on temperature dependence of critical current peaks in $FeTe_{0.60}Se_{0.40}$ - Silver point contacts in the thermal regime.	28
2.10	Dependence of critical current peaks in $FeTe_{0.60}Se_{0.40}$ - Silver point contacts on external magnetic fields.	29
2.11	Periodic spikes appeared in the differential resistance spectra of $FeTe_{0.60}Se_{0.40}$ -silver point contacts at low magnetic fields from 100 to 300 Oersted. Magnetic field was increased in steps of 50 Oersted from 0 to 300 Oersted.	29
2.12	Close up view of the niobium tip facing the gold film. 0.1mm Gold wire contacts on the sample have been mounted using silver epoxy.	30
2.13	PCAR spectra of Niobium-Gold point contact	30

Chapter 1

Scanning Tunnelling Microscopy

Scanning Tunnelling microscopy has been long established as a powerful tool for imaging electrically conducting surfaces down to atomic length scales. It functions by raster scanning a sharp probing tip in close proximity to the sample over the XY plane. As opposed to optical microscopes that can visualize an entire area at once by mapping the intensity of photons, scanning tunnelling microscopes work by calculating the tunnelling current flow between the sample and the tip, and must move the tip to each point on the area and track the tip height variation in order to obtain a 3D image corresponding to the topography (Daub 2010).

The broad range of capabilities of Scanning Tunnelling Microscopes have made them a very powerful tool in all the major sciences.

1.1 Review of Scanning Tunnelling Microscopes

The concept of Scanning Tunnelling Microscopy as we know it today, was the result of a collaborative effort by Gerd Binnig and Heinrich Rohrer who were working at the IBM Zurich research laboratory in the late 70s. Their invention enabled scientists to visualize surfaces all the way down to atoms and molecules for the first time, and they were awarded the Nobel Prize in Physics in 1986 for it (Chen 2008). Investigation of the crystal structure of gold with this device was their first successful experiment, and they reported their observation of atomic lattices, as well as broad terraces (Binnig et al. 1982).

The essential components of an STM include a sharp probing tip, a coarse approach mechanism capable of reducing distances to down to the order of micrometres, and a piezo-electric material based fine approach mechanism capable of lateral as well as axial motion with sub-angstroms resolution. The hardware is complemented with the necessary electronics, chief among them being a preamplifier with a working range of $< 10pA$ to $10nA$ which is coupled with a feedback loop that maintains a constant tunnelling current by dynamically

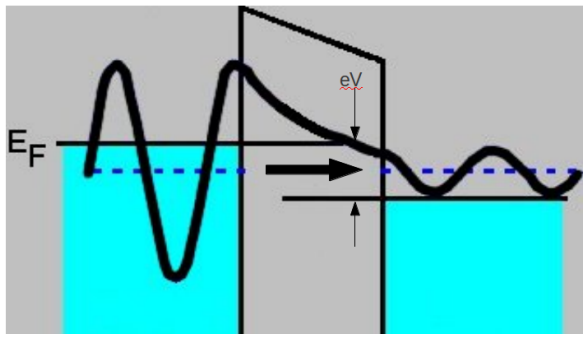


Figure 1.1: Schematic diagram of the electronic wave-function as it tunnels through a physical barrier. The sample's Fermi level has been modified by applying an external bias.

changing the tip-sample separation via the piezoelectric scanning tube. A vibration isolation stage is necessary because the tip-sample distance is of the order of an Angstrom , and this makes the tunnelling current extremely sensitive to vibration (Okano et al. 1987).

Modern day STMs are set up under ultra-high vacuum chambers inside low-temperature cryostats. Such systems are free from thermal noise, and have minimal interference from gas molecules (Assig et al. 2013).

1.1.1 Electron tunnelling

Classical mechanics forbids a particle incident on a barrier from crossing over if it does not have sufficient energy to scale it. It will therefore be reflected with unity probability.

Quantum mechanics however, predicts a finite probability of the particle tunnelling over to the other side. This can be interpreted in relation to the wave nature of the electrons, and the Heisenberg uncertainty principle. The wave function contains information about the particle in question in a given physical system. Calculations concerning the behaviour of the particle primarily involve solving the wave function. In the case of simple rectangular potential barriers, the wave function can be analytically solved using the Schrödinger wave equation in order to obtain the probability density of the particle's position (Probst 2002).

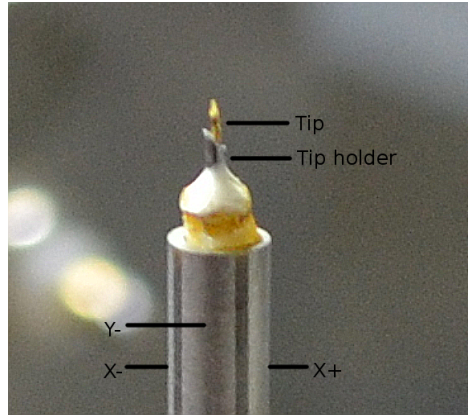


Figure 1.2: Scan-tube with axially segmented electrodes. Potential difference applied to the electrodes causes the relevant sections to expand, and this is used to flex or expand the whole tube.

STMs utilize the concept of electron tunnelling which results in a finite current flow when a potential difference is applied between two conducting surfaces separated by a thin insulating barrier with thickness less than a few nanometres (Chen 2008) . Commonly, the sample is biased with a voltage(V), and the tip is virtually grounded. For a positive bias, electrons tunnel from the occupied states in the tip, to the empty states in the sample.

The tunneling current is exponentially sensitive to the separation of the barrier, and this is crucial in ensuring an excellent lateral resolution as the tunneling current is carried by the outermost atom on the tip. The contribution from the neighbouring atoms is negligible, and as a result the scanning is carried out by a single atom (Redinger 1998). Sharp tips can therefore be easily prepared by cutting a wire, or by etching.

1.1.2 Piezoceramic based fine approach and scanning

Piezoceramics are commonly used in applications where mechanical movement with subatomic resolution is required. The ability of such materials to expand/contract in response to the smallest changes in the potential difference applied across them plays a very important role in the success of scanning probe microscopy (Vieira 1986).

Piezoceramics in the shape of tubes are frequently used in scanning probe microscopy since a single tube can be used to handle motion of the tip in all three directions using appropriately designed electrodes (Lee et al. 1997). A common configuration is to coat the inner surface with an electrode that is grounded, and four axially segmented electrodes on the outer surface are connected to independent high voltage amplifiers (Taylor 1993). Figure 1.2 shows our setup with a gold tip mounted on the scan-tube.

1.1.3 Constant current operation

The constant current mode, as the name suggests, involves maintaining the tunneling current at a constant value. This is achieved using a feedback loop that controls the tip-sample separation based on the tunneling current value.

A bias voltage is applied to either the tip, or the sample, and the other is connected to a preamplifier which amplifies the tunneling current flow. Since this current is usually of the order of a few hundred picoamperes, a current sensitive pre-amplifier stage with a high gain of the order of $1V/nA$ is attached very close to the source. Minimizing the distance travelled by the original signal is imperative in order to prevent noise from making it unusable before it reaches the pre-amplifier.

Once the tip sample separation has been brought into the tunneling domain, the electronic feedback mechanism maintains a pre-set, user-configurable separation by dynamically making corrections to the voltage offset applied to the scantube. If the tunneling current falls below the preset value, the separation is reduced by expanding the scantube, and if it exceeds the preset, the separation is increased by contracting the scantube. therefore, a constant tunneling current is maintained.

The voltage correction that needs to be made to the scantube is algorithmically calculated by studying the variation of tunneling current over a short time period. The correction is the sum of the error signal times the proportional gain, and the integral of the error signal times the integral gain.

Such a feedback loop is appropriately called a Proportional-integral(PI) loop.

The values of integral and proportional gain that must be set manually , are dependent upon various parameters such as surface roughness, set-point, scan speed, and bias voltage.

A higher surface roughness may warrant using a higher integral gain in comparison with a smoother surface scanned at the same speed, but this comes at the cost of loss in z-resolution due to overshoot errors from the feedback loop.

The procedure for obtaining raster scans of the topography is now quite straightforward via a method appropriately named as *constant current scanning mode*.

Adjusting the voltage levels on a quadrant electrode of the scan tube has the effect of bending the tube in a direction normal to that quadrant. This property is used to move the tip over the surface while the feedback loop continuously adjusts the voltage offset in order to maintain a constant tunneling current. The value of the offset is mapped as a function of the lateral position of the tip, and this directly reflects the topography of the sample being scanned.

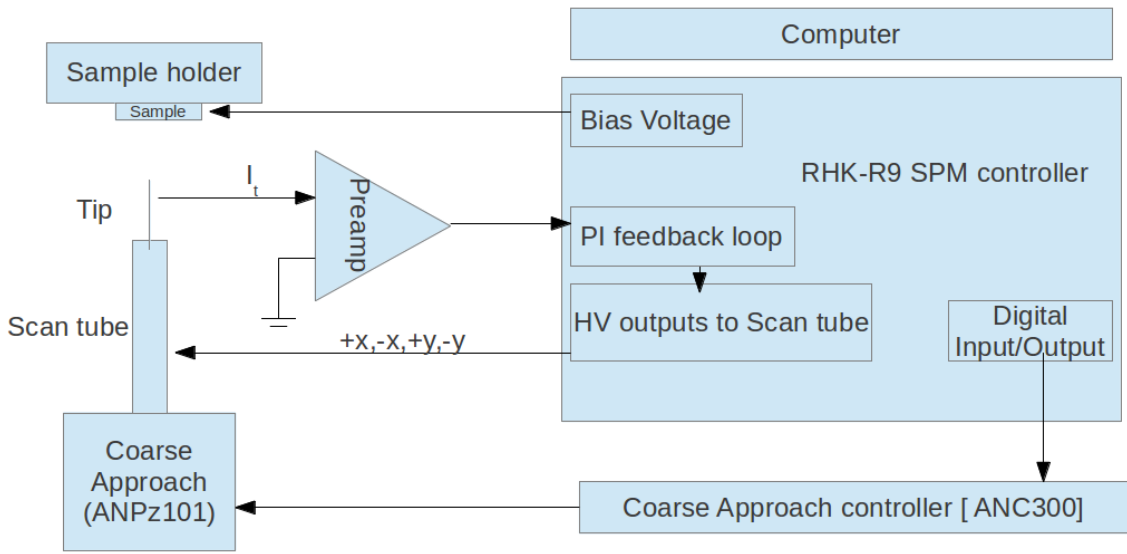


Figure 1.3: Flowchart indicating the control and data flow between various components of the STM

1.1.4 Constant height operation

Another mode of operation is the *constant height mode*, and this involves turning off the feedback loop and obtaining a map of the tunneling current. In the absence of the feedback loop, the tunneling current is a function of the tip-sample separation which varies as the tip moves over the topography. A frozen feedback loop also means that this mode is only possible for small areas which are extremely flat, as otherwise the tip may crash into the sample, or exit the tunneling domain.

For piezo-tube based scanners, the bending method used for scanning results in an offset proportional to the radial distance of the tip from the centre of the total scan area being added to the tip-sample separation. This causes constant height images to have a convex appearance.

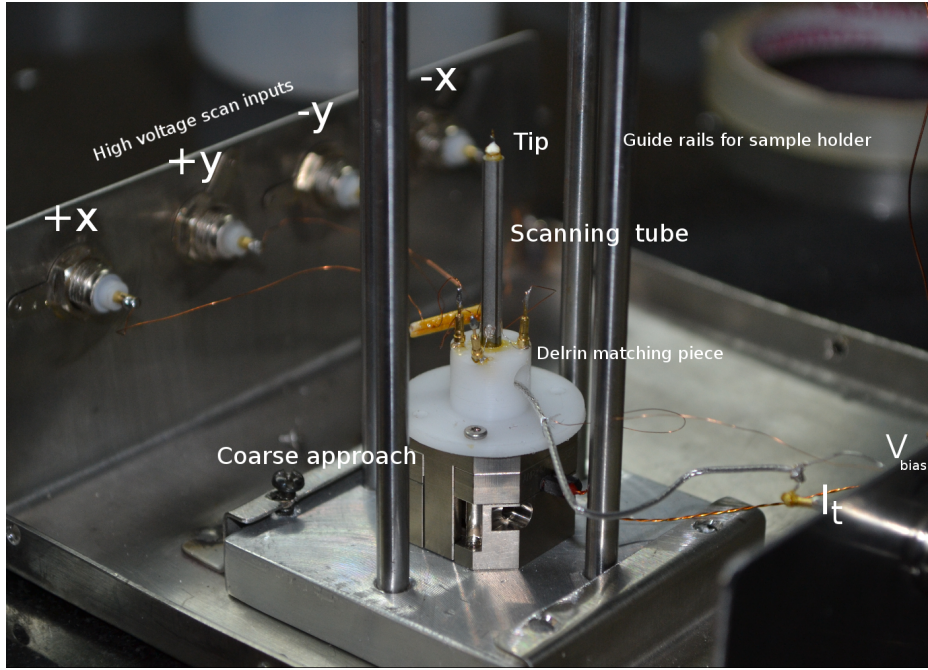


Figure 1.4: Various parts of the room-temperature STM's hardware.

1.2 Development of a room temperature STM

The presented work on Scanning tunneling Microscopes involved the design and testing of a prototype device at room temperature using components compatible with low temperatures, and high vacuum.

1.2.1 Hardware

The STM assembly consisting of a coarse approach, scan tube, and sample holder has been housed in a container machined out of Stainless steel in order to block out Radio-frequency noise. Standard BNC connectors have been mounted on this case, and are used to make connections to the scan tube, tip, and sample holder. The coarse approach signals are fed through a coaxial copper wire. A rail mounted sample holder enables the user to visually adjust the tip sample distance to less than a millimetre, following which automatic coarse approach can be activated.

The entire assembly was suspended using bungee cords from the roof of an instrument rack in order to attenuate mechanical vibrations and reduce interference from ambient acoustic noise.

Coarse approach mechanism

Coarse approach is handled by a slip-stick style nano-positioner(ANPz101) manufactured by Attocube Systems. This device has a titanium body, and a footprint of $24mm \times 24mm$. It is capable of a maximum vertical travel range of $5mm$, and does so by taking steps less than a micron in length (systems 2010). It requires an input sawtooth waveform to move, and while the height of the waveform decides the step size, its direction decides the travel direction. The large capacitance of the stack piezo used inside the positioner, and the extremely short rise/fall times of the electrical pulses required for operating it implies a large current flow. This can be calculated to be around 10 amperes for a 20 V pulse that rises to 90% of its value within $2\mu s$ when applied to a nano-positioner with $1\mu F$ capacitance. Since the high voltage outputs of the R-9 cannot drive such high capacitance loads, a dedicated controller, ANC-300 with an ANM-150 stepping module was used to drive the coarse positioner. It is triggered via digital I/O channels controlled by the R-9. This device is capable of working at cryogenic temperatures, and under high vacuum.

Fine approach, and scanning tube

A piezo tube made of PZT-5H(Lead Zirconate Titanate based piezoceramic) manufactured by Physik Instrumente (“Pt120 - pt140”) is used as the lateral scanner, as well as for varying the tip-sample distance with picometre resolution. It has an inner electrode made of fired silver, and this is connected to ground. The outer electrode is made of Cupro-Nickel, and is axially segmented into four quadrants called X+, Y+, X-, and Y- based on the direction the tube bends when a positive voltage is applied to one of them. Each quadrant is connected to a separate high voltage amplifier, and the tube can be bent by upto $35\mu m$ in each direction by applying voltages upto 200V. Expansion in the Z direction can be controlled by summing a uniform voltage into all four electrodes, and a maximum expansion of $9\mu m$ can be achieved.

Tip holder

A section of a 0.3mm Inner diameter hypodermic needle is used as a tip holder. This is attached on the scanning end of the piezo tube via an insulating matching piece. Tips are made by clipping 0.25mm wires, and these are push fitted into the needle after making a small kink to hold them tight. The tunneling current is carried by a coaxial wire of 1mm diameter which passes through the scan tube, and emerges from the side of the scan tube pedestal machined in Delrin. The shield of this wire is attached to the inner electrode of the scan tube, and is grounded.

1.2.2 Approach procedures

Before scanning process can be initiated, the tip needs to be brought within range of a few angstroms from the sample in order to establish a tunneling current. Once this separation has been visually adjusted to around a millimetre, an elaborate collaboration between the coarse approach mechanism and the scan tube is used to reduce this separation and bring it into the tunneling range.

Each step of the coarse approach may be as large as a micron. This implies that a single step can move the tip from outside the tunneling distance to establishing an ohmic contact and destroying the tip. The total extension range of the scan tube is a few microns, and using just the scan tube for establishing tunneling current after visually adjusting the tip-sample separation to within its maximum range is not practical. Therefore, a combination of the coarse approach, and scan tube must be used, and the only constraints being that the extension range of the scan tube be greater than the step size of the coarse approach motor, and that the starting separation be within the total travel range of the coarse approach mechanism.

Approach is carried out by a series of steps that are repeated until a tunneling current is established.

First, the scan tube is retracted to its shortest length. Following this, the coarse approach takes a single step. Since the coarse step is shorter than the contraction of the scan tube, the tip is safely away from the sample. Following this, the scan tube is slowly expanded linearly, and the tunneling current signal is continuously monitored. If the tube reaches its maximum limit without any tunneling current being observed, it is retracted again, and the procedure is repeated. A plot of the voltage applied to the piezo tube during the approach mechanism is shown in Figure 1.5 . The convention of this setup is taken such that a positive value of the piezo length indicates a greater tip-sample separation.

1.3 Software

The entire assembly was controlled using a program developed in the Iconic Hardware Description Language(IHDL) . This architecture allows easy construction of STM control programs based on configurable components that can be real (A/D, D/A convertors, I/O ports etc.) or virtual (feedback loops, Phase locked loops , scan generators etc.) . Critical, low-latency procedures such as feedback loops are downloaded onto Field Programmable Gate Arrays(FPGA) on the hardware , and are linked to relevant electronics such as A/D convertors and high voltage amplifiers. FPGAs contain large arrays of logic gates and Read Only Memory blocks on which Application Specific Integrated Circuits can be implemented by downloading programs written in a Hardware Description Language(HDL). Once they have

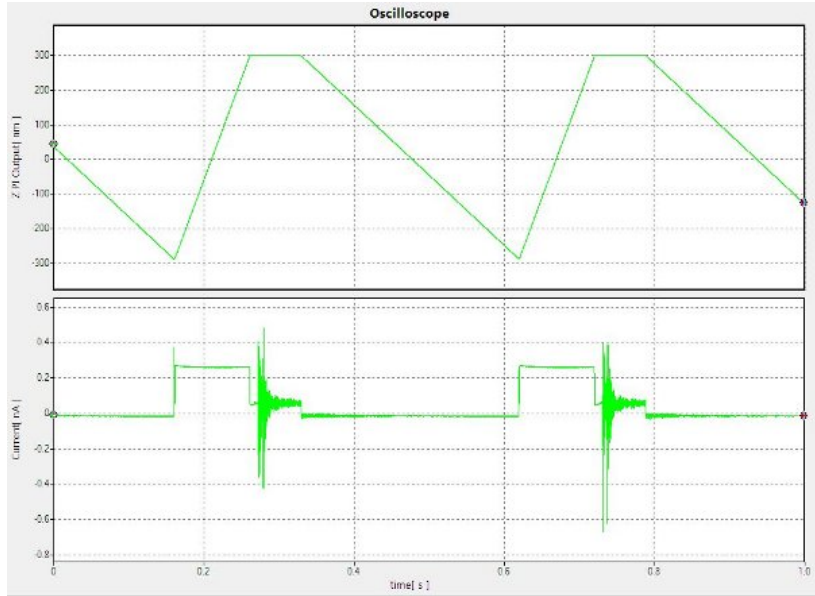


Figure 1.5: Top) Waveform applied to the scan tube during coarse approach. Bottom) tunneling current signals indicating the stepping noise generated by the coarse approach motor, and the induced current from the scanning voltage.

been programmed, they behave like dedicated Integrated Circuits(IC) (Bhatia 1996).

The R-9 software was also used for image manipulation such as slope correction, and line extraction.

1.3.1 Calibration of scan ranges using a standard sample

STMs deal with length scales represented as a function of the voltages applied to the scan tube. The scale of the scans obtained thus have no meaning until the deflection is measured in standard units of length which are a function of the voltage. In order to do this, several images were obtained on a standard metallic calibration grating (CalibratAR 3D calibration reference) manufactured by Asylum Research(Figure 1.6) (“3D Calibration Reference”). This sample consists of a grid of $200\text{nm} \pm 4\text{nm}$ depth square pits with sides of $5\mu\text{m}$ each, and an X and Y pitch of $10\mu\text{m} \pm 0.04\mu\text{m}$ each.

Before acquiring these scans(Figure 1.7), approximate calibration data was calculated from physical property data provided by Physik Instrumente which manufactured the scan tube was and used. The XY travel range was specified as $35\mu\text{m}$ at 200V , and maximum Z expansion was given as $9\mu\text{m}$. This corresponds to a lateral deflection of 175nm/V , and expansion of 45nm/V .

From Figure 1.8, the lateral deflection can be estimated to be around $5\mu\text{m}$, and a conversion factor of 175nm/V is obtained.

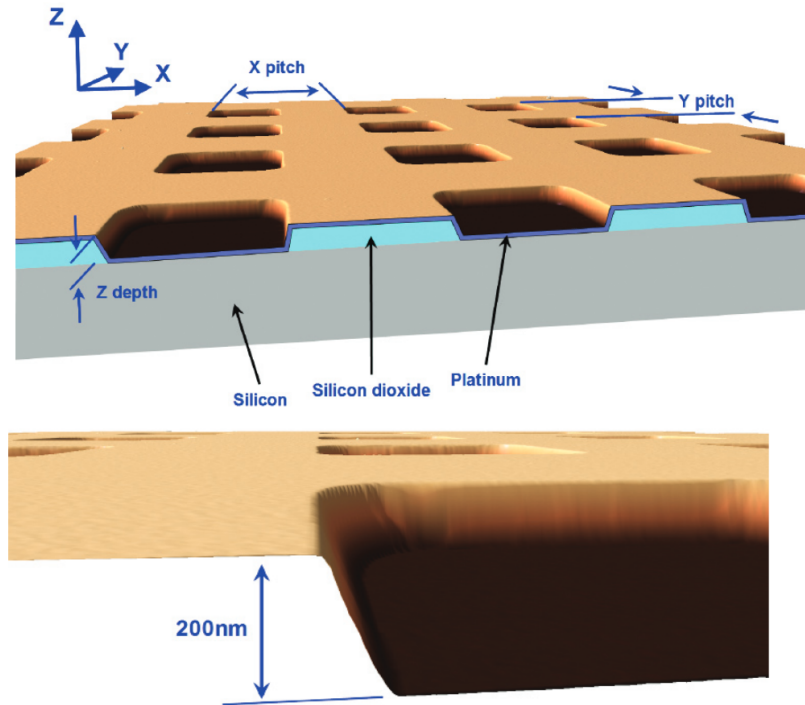


Figure 1.6: Technical drawing of the calibration grating used (Courtesy : Asylum Research) (“3D Calibration Reference”). Key features are a lateral pitch of $10\mu m \pm 0.04\mu m$ and depth of $200nm \pm 4nm$

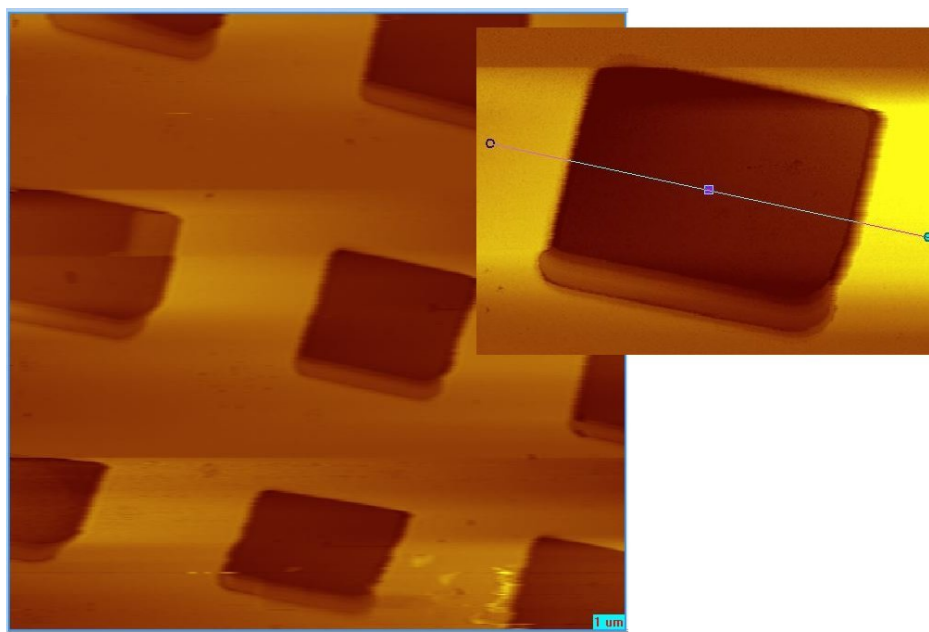


Figure 1.7: Topographic image of a calibration grating obtained using the STM . Inset: High-res scan of a single pit, with a line depicting the route over which depth information was extracted and has been plotted.

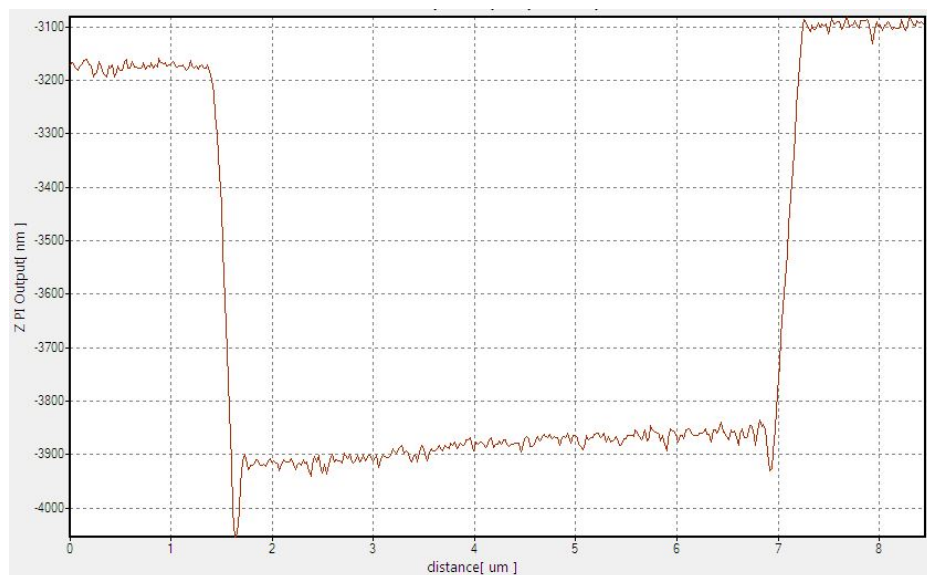


Figure 1.8: Depth profile of a single pit on the calibration grating. A depth of $\sim 700\text{nm}$, and a width of $\sim 5\text{um}$ can be seen.

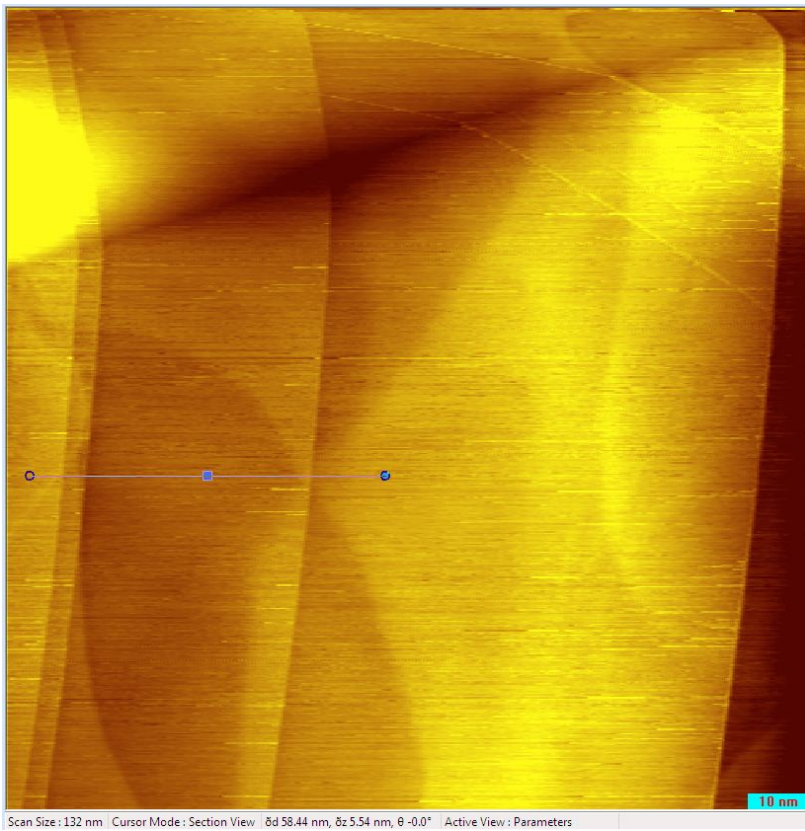


Figure 1.9: a $100\text{nm} \times 100\text{nm}$ scan on HOPG showing atomic layers.

1.3.2 Measurements on *Highly Oriented Pyrolytic Graphite*

Highly Oriented Pyrolytic Graphite(HOPG) is a form of high purity carbon, and has the familiar layered structure of graphite. It is one of the preferred materials for testing as well as calibrating tunneling microscopes at room temperatures due to the ease with which it can be cleaved to obtain a pristine surface, and its readiness to provide "atomic" resolution.

$100\text{nm} \times 100\text{nm}$ scans(Figure 1.10) were obtained on a freshly cleaved HOPG sample manufactured by SPI supplies, and the presence of several steps of around $\sim 100\text{pm}$ in the extracted depth profile confirmed the presence of single atomic layer boundaries.

1.3.3 Scanning tunneling spectroscopy

Scanning tunneling microscopes can be used to obtain tunneling current vs bias spectra in order to probe the local electronic structure of materials over extremely small areas. The feedback loop is frozen, and the tunneling current is recorded as a function of the bias voltage swept over the desired range. Figure 1.11 shows the I-V characteristics of HOPG.

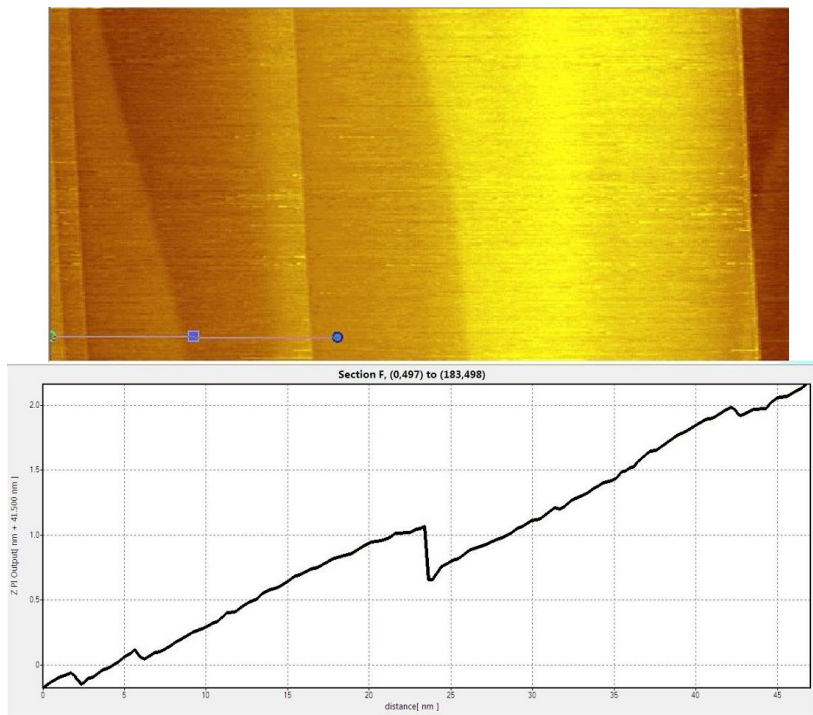


Figure 1.10: a $100\text{nm} \times 100\text{nm}$ scan on HOPG showing layer boundaries.

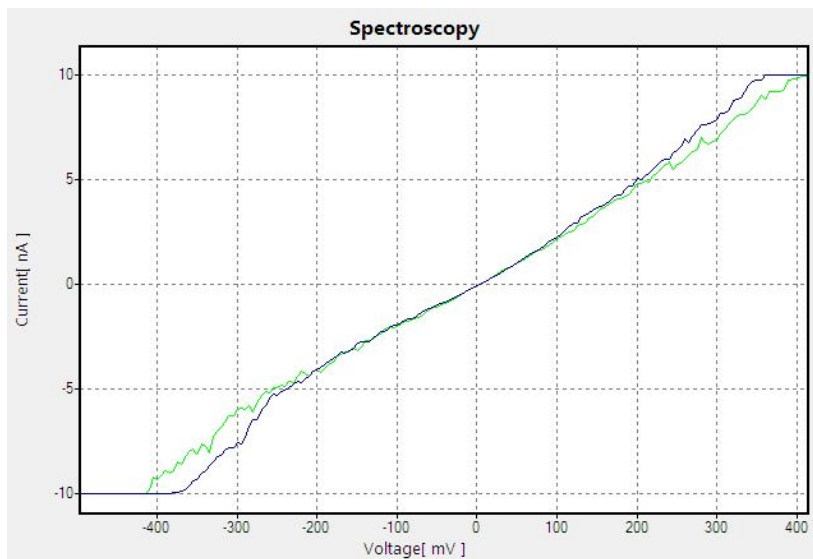


Figure 1.11: I-V spectroscopy on HOPG.

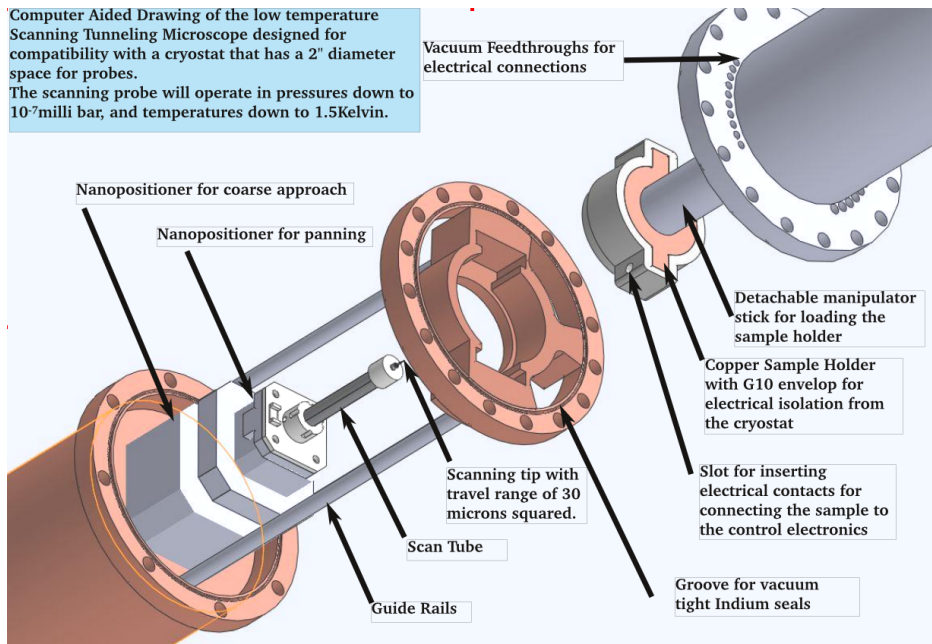


Figure 1.12: Exploded view of the STM section of the cryostat insert designed using Solidworks.

1.4 Designing a low-temperature STM

Following up with the tested room-temperature prototype, the next step is to design and develop a low-temperature STM compatible with a 2" bore liquid helium cryostat.

A schematic was designed using Solidworks for developing an ultra-high vacuum STM. Nanopositioners have been chosen for coarse approach and panning, and Macor ceramic parts are used to mount the scantube.

The cryostat uses a dynamic variable temperature insert(VTI) for further cooling samples down to 2 Kelvin. This is achieved using a Joule-Thomson needle valve that draws helium and allows it to expand inside into the VTI. To prevent gas molecules from interfering with scans, a separate vacuum chamber is required to isolate the scanning assembly. The design contains two Indium sealed flanges in order to allow the microscope to be detached from the long chamber easily.

The sample holder can be attached to the cold microscope using a manipulator stick inserted using a load-lock mechanism. Load-lock involves using a two stage valve through which the manipulator must pass to prevent inflow of air that will condense when it reaches the microscope maintained at liquid helium temperatures. The holder is covered by an electrically isolating material(G-10), since it must be virtually grounded and not touch the cryostat body.

Chapter 2

Point Contact Andreev Reflection Spectroscopy

2.1 Electronic transport across nano-constrictions

Contacts between conductors can be classified based on their radius , and the smallest radius possible for a conducting pathway is limited by the de-Broglie wavelength of the electron (Topinka 2000). Electrons flowing through conductors wider than the mean free path routinely undergo scattering by phonons and other elementary excitations, but the current-voltage characteristics of this form of transport, commonly known as bulk transport, is the result of scattering of these electrons whose momenta are spread out over the Fermi surface. Instead, when a nano-constriction with width less than the mean free path is used, statistically speaking the electrons can be assumed to undergo zero scattering (Nikolic and Allen 1998). In such a case, the kinetic energies of electrons being scattered can be defined as a function of the potential difference(V) across the constriction. This allows energy resolved spectroscopy of the elementary excitations by measuring the current-voltage characteristics of such a junction (Jansen, Gelder, and Wyder 1980).

The "Needle-Anvil" method employed by our instrument setup is the simplest for forming nano-constrictions (Janson et al. 2012). A needle like conductor is brought into contact with a flat conductor using a precise mechanical assembly to make cracks in existing oxide layers resulting in the formation of conduction pathway of a very small radius. The resulting point-contact acts as a local probe, wherein the electrical transport is affected by the scattering processes occurring within the local neighbourhood of the contact (Erts et al. 2000).

Conductance varies from the Sharvin regime for purely ballistic contacts to the Maxwell regime for bulk transport (Nikolic and Allen 1998). Purely diffusive contacts are described by the Ohm's Law, where resistance is given as a function of the resistivity, the area of cross

section, and the length of the conductor.

Conductance across contacts can be compared with the problem of gas flowing between two chambers with unequal pressures via a small orifice. When the dimensions of the orifice(a) are less than the path length(l) of the gas molecules, diffusive flow assumptions are no longer valid, and ballistic transport occurs. This problem was first studied by Knudsen(1984), and the Knudsen ratio (l/a) is used to describe the various transport regimes.

2.1.1 Thermal regime

For current flowing through a metallic contact with radius much greater than the mean free path, current-voltage characteristics are linear, and are described by the Ohm's law. The Maxwellian resistance for such a contact obtained from the solution of Poisson's equation and Ohm's law is given by $[R_M = \frac{\rho}{2a}]$.

2.1.2 Ballistic regime

When the size of the contact is much greater than the de-Broglie wavelength of the electron, but is smaller than the elastic scattering mean free path, the contact can be described as ballistic one. Ohm's law is no longer valid for such a contact. In terms of the Knudsen ratio, $l/a > 1$.

Application of a potential difference across such a contact results in a large potential gradient in a small region across the contact. This causes electrons near the contact to be accelerated, and gain sufficient energy to move across it.

The velocity gained (δv) by an electron accelerated across the contact is proportional to the potential difference across it ($\delta v = \frac{eV}{p_f}$) where p_f is the fermi momentum.

The current through such a contact is given by

$$I \propto \pi a^2 \frac{n_o e^2}{p_F} V \quad (2.1)$$

where n_o is the electron density. Using the Drude formula for resistivity, $\rho = \frac{p_F}{n_o e^2 l}$, the Sharvin resistance in the ballistic limit is found to be

$$R_s \propto \frac{\rho l}{\pi a^2} \quad (2.2)$$

Integrating over all possible incident angles introduces a factor of $\frac{4}{3}$. The Sharvin resistance for a circular contact in the ballistic limit is therefore given by $R_s = \frac{4\rho l}{3\pi a^2}$.

Sharvin resistance is independent of the mean free path, since $\rho \propto 1/l$

2.1.3 Interpolation of Sharvin and Maxwell Regime

In between the limiting cases of purely ballistic, and purely thermal regimes, Wexler gave the expression for an interpolation (Wexler 1966),

$$R = \frac{4}{3\pi} \frac{\rho l}{a^2} + \Gamma(K) \frac{\rho}{2a} = \frac{4}{3\pi} \frac{\rho l}{a^2} \left(1 + \frac{3\pi}{8} \Gamma(K) \frac{a}{l}\right) \quad (2.3)$$

Where $\Gamma(K)$ is a slowly varying function of the Knudsen number , K . The factor $[\frac{4}{3\pi} \frac{\rho l}{a^2}]$ is the Sharvin resistance.

2.1.4 Critical current in nano-constrictions

Superconductors, while normally exhibit zero resistance below their transition temperature, turn resistive when the current density flowing through them exceeds a certain limit. This is known as the critical current density, and its effects are visible in point contact spectra in the form of additional potential difference generated when critical current density is reached, and the nano-junction turns resistive. These appear as peaks in the differential resistance curves, and are symmetric upon current reversal. During experiments, multiple peaks may occur when as many contacts with different geometries are formed.

2.1.5 Blonder, Tinkham, Klapwijk formalism for Andreev reflection in Normal metal - superconductor nano-junctions

Blonder, Tinkham, Klapwijk proposed a theory (Blonder, Tinkham, and Klapwijk 1982) for modelling the current-voltage characteristics in normal metal - Superconductor micro-constrictions. Their formalism includes a barrier potential parameter(z) which can be varied from the pure tunneling (N-I-S) regime to the contact regime (N-S) where ballistic transport occurs.

They use the Bogoliubov de-Gennes equations to treat the transmission and reflectance of particles at the N-S boundary within a generalized semiconductor model.

This formalism describes the probabilities for the various outcomes that may occur when an electron is incident at the N-S boundary. The dependence of these probabilities on incident energy is plotted in figure 2.1 . The various probabilities are,

- (A)Andreev reflection - $\frac{\Delta^2}{E^2+(\Delta^2-E^2)(1+2Z^2)^2}$ for $E < \Delta$ which tends to unity in the zero barrier limit , and $\frac{\mu_o^2 v_o^2}{\gamma^2}$ for $E > \Delta$
- (B)Ordinary reflection - $1 - A$ for $E < \Delta$ which tends to zero for a ballistic contact , and $\frac{(\mu_o^2 - v_o^2)^2 Z^2 (1+Z^2)}{\gamma^2}$ for $E > \Delta$

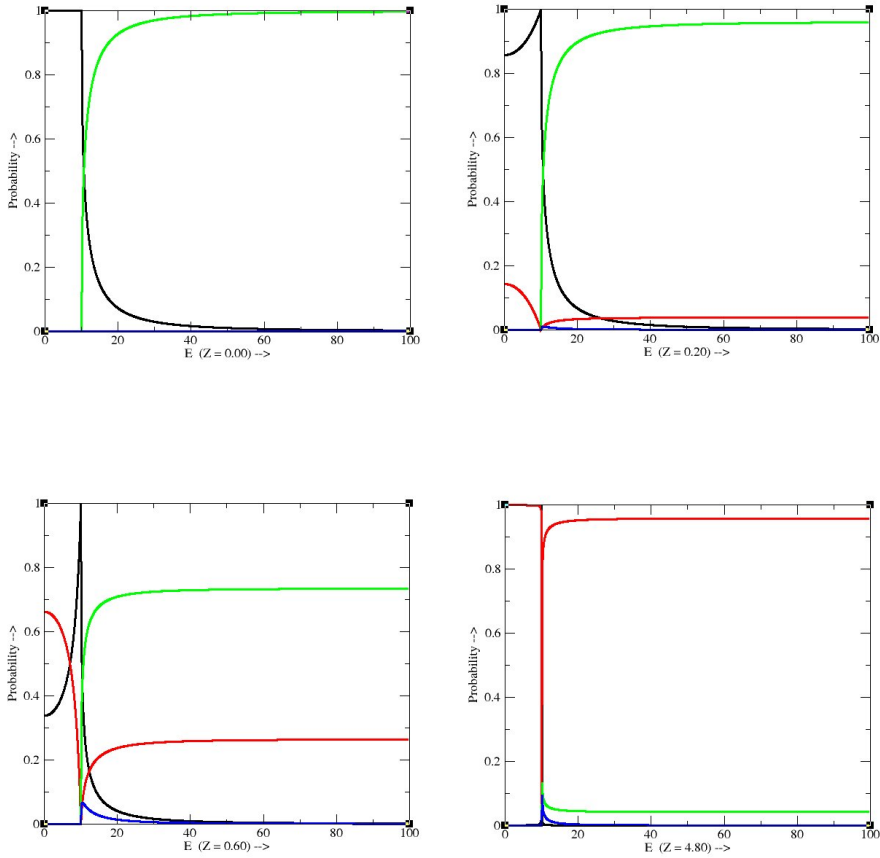


Figure 2.1: Transmission and reflectance probabilities plotted for transport across an N-S junction with the energy gap of $S(\Delta) = 2meV$, and different values of the barrier potential($0, 0.2, 0.6, 4.8$).

- (C)Transmission with branch crossing - 0 for $E < \Delta$, and $\frac{\mu_o^2(\mu_o^2-v_o^2)^2Z^2}{\gamma^2}$ for $E > \Delta$
- (D)Transmission without branch crossing - 0 for $E < \Delta$, and $\frac{v_o^2(\mu_o^2-v_o^2)^2Z^2}{\gamma^2}$ for $E > \Delta$

The current across an N-S boundary for a superconductor with an energy gap Δ at a temperature T and bias V can be obtained in terms of these probability distribution functions, and the fermi distribution functions for electrons incident from the Normal metal side ($f_o(E - eV)$) and those from the superconducting side $f_o(E)$.

$$I_{NS} = 2N(0)eVFA \int_{-\infty}^{\infty} [(f_o(E - eV) - f_o(E))(1 + A(E) - B(E))]dE \quad (2.4)$$

2.2 Differential conductance

Differential conductance is one of the most critical measurements for characterising non-linear properties of nano-scale electrical junctions at low-temperatures. It involves calculating local slopes of the current-voltage dependence of the junction. The values obtained can be used to extract information about properties such as band gaps and barrier thickness using appropriate curve fitting with known theoretical predictions.

In the present scenario, a ballistic point contact between a normal metal and a superconductor is made. Differential conductance measurements below critical temperature on such a junction shows two peaks on either side of neutral bias for a finite barrier thickness. These peaks merge to form a plateau if the barrier is transparent. This data can then be fitted with equations from the BTK theory in order to obtain the superconducting band gap.

There are several methods to obtain differential conductance, a common few are,

- Carrying out a current-Voltage sweep, and then mathematically calculating the derivative. This may also include using a moving average of datapoints in order to reduce the effect of noise
- Use a DC offset sine wave to carry out measurements, and then use Lock-In amplifiers to extract the voltage and current across the device being tested.

Current-Voltage sweep technique

I-V sweep can be described as the most simple technique to set up, but the limitations it faces makes it one of the least favoured when it comes to taking measurements on sensitive devices at low temperatures. Noise is greatly amplified when derivatives are taken, and may be unacceptably large for most cases. Therefore, Several I-V sweeps need to be acquired in order to reduce noise by a factor of \sqrt{N} where N is the number of times each datapoint was acquired (Simson 1987). This technique can also have disastrous consequences due to Joule heating when large current sweeps are carried out on nano-scale devices. Even for small currents, the temperature difference generated decreases the credibility of the data.

Modulated DC-bias technique

This technique provides a much lower noise floor, and is frequently employed for differential conductance measurements. A DC bias voltage is mixed with a small amplitude sinusoidal signal of known frequency using a summing amplifier, and applied to the sample. The measured signal is then multiplied with the original AC signal, and integrated over an appropriate time period. This returns a clean DC signal, since periodic noise averages to zero (**Lock-in amplifier**).

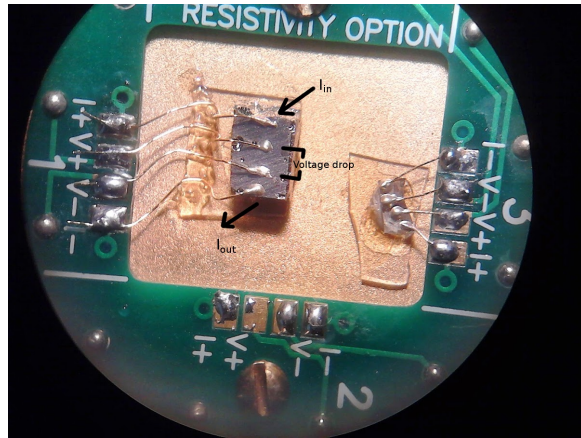


Figure 2.2: Four probe connections made to a sample for measurements with a Physical Property Measurement System

For low frequency noise, a larger integration time needs to be employed, and this increases the measurement time. A faster modulation frequency may be used, but this speed is limited by the RC time constant of the setup, where R is the device impedance, and C is the cable capacitance.

The modulated bias technique also suffers from limitations related to Joule heating.

2.2.1 Measurement with a Pulsed Differential resistance setup

The pulsed I-V technique involves using a current source(Keithley 6221) capable of switching pulses down to 100 microseconds in width, and a nanovoltmeter(Keithley 2182a) that can be triggered by the current source whenever measurements need to be obtained (“Low-Level Pulsed Electrical Characterization with the Model 6221 / 2182A Combination”). Connections are made to the device in the standard four-probe way.

In this technique, A staircase current sweep is summed with a known alternating current offset pulse (dI). The current source is synchronized with the nanovoltmeter using a trigger cable, and the voltage is calculated for each step with the offset pulse off, and then on. The setup then calculates dV for each step, and stores the differential conductance dataset which may be retrieved manually or via a computer. Such a pulsed technique enables low noise data acquisition without the need for several sweeps.

The acquisition parameters such as the step height, pulse widths, delta height, and range can all be customized.

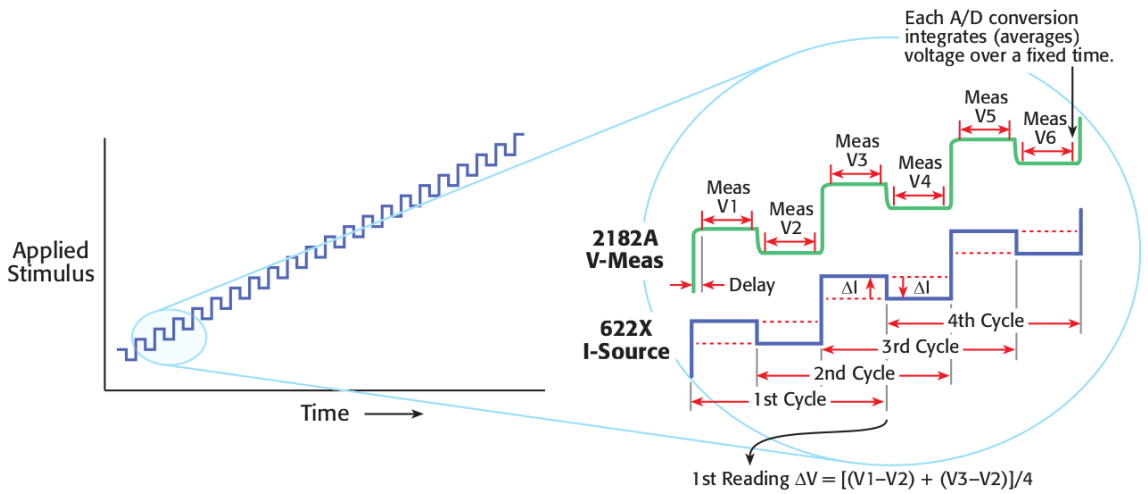


Figure 2.3: a) The current pulses applied during pulsed differential resistance measurements
b) Detailed view of the acquisition technique. Source: 2610, White paper on differential conductance measurements

2.2.2 Measurements with a Pulsed Delta setup

The pulsed delta setup differs from the differential resistance technique mentioned in the previous section in that it does not use a linearly increasing current staircase at all. It acquires a current-voltage curve using short current pulses.

Pulses as short as 100 microseconds are fired from zero amperes to the required amount, and the voltage is measured after allowing a small settling delay for the pulse. Voltage is measured in the off state too, and dV is calculated. An off state delay can be programmed between each pulse in order to allow the sample to cool. This is advantageous for use with sensitive devices which can heat up rapidly due to low cooling rates

The I-V curve obtained must be differentiated point-wise after acquisition in order to calculate the differential conductance.

2.3 Construction of a point contact spectroscopy probe

A point contact spectroscopy probe was developed in-house in order to carry out differential conductance measurements at low temperatures. It was designed to be compatible with both a 1" cryostat of a (*Physical property measurement system(PPMS)*), as well as a 2" cryostat from American Magnetics. The data acquisition setup used the pulsed differential conductance technique based on an AC/DC current source(Model-6221), and a NanoVoltmeter(Model-2182a) from Keithley Inc. A Model-350 temperature controller

from Lakeshore Inc was used to monitor and control the sample temperature. Andreev reflection spectroscopic data was acquired using a Niobium-Gold point contact prepared with this probe and the PPMS cryostat. The same setup was used to study the dependence of critical current in an $FeTe_{.60}Se_{.40}$ - Silver point contact on temperatures down to 2 Kelvin, as well as magnetic fields upto 3 Tesla. Sample heating as a function of measurement current was also determined in real time in order to increase the credibility of acquired data.

2.3.1 Mechanical structure

In order to carry out point contact spectroscopy, the probe should be designed to fit into a cryostat, and must have necessary feedthroughs to vary the radius of the contact in-situ, as well as carry electrical signals.

Keeping these requirements in mind, an appropriate probe was designed.

Four hermetically sealed electrical connectors were prepared which could be attached to matching flanges on the probe.

A hypodermic needle was used as a tip holder, and this was attached to a 100t.p.i. differential screw using a matching piece machined out of Delrin(machinable plastic). In order to move the tip back and forth, the differential screw must be rotated, and it was therefore attached to a stepper motor located on the room-temperature end of the probe by means of a long shaft that is hermetically sealed using a compressed O-ring. The stepper motor is capable of making a single rotation in 360 discrete steps, and combined with the hundred turns per inch pitch of the screw, the tip can be moved in steps of approximately 30 microns.

To minimize heat flow from the warm end of the probe to the cold end, all connecting rods were made of stainless steel. Electrical connections were made using thin, 42 gauge, insulated copper wires for minimizing heat flow. These were wrapped using Teflon tape for protection.

The differential screw was housed in a brass assembly, and a sample holder machined out of copper was mounted against the tip holder by using three stainless steel posts screwed into the brass assembly(figure 2.5).

2.3.2 Wiring and electronics

Electrical wiring inside the probe was carried out using thin, 42 gauge, insulated twisted pair copper wires for minimizing heat flow. These were wrapped using Teflon tape for protection. Twisted pairs cancel noise from fluctuating magnetic fields generated by current flowing through them.

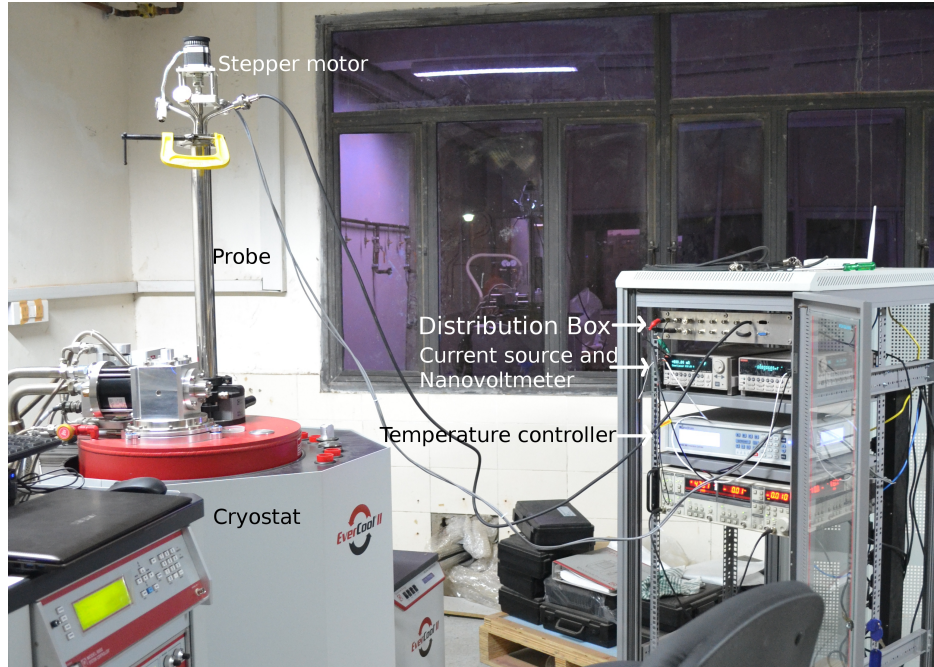


Figure 2.4: The probe mounted on a PPMS cryostat, and connected the acquisition instruments. The additional length of the probe was provided in order to make it compatible with a deeper cryostat.

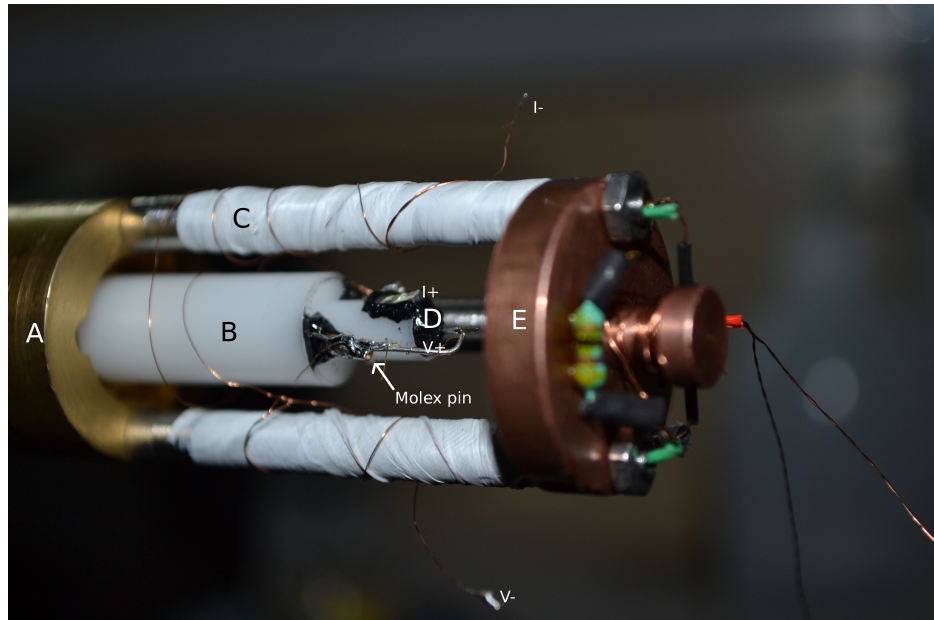


Figure 2.5: The cold end of the probe. A) Brass holder containing the 100t.p.i. screw. B) Delrin extender for mounting the tip holder. C) Stainless steel mounting posts D) Hypodermic needle based tip-holder fixed using Stycast epoxy adhesive E) Sample holder machined in Copper.

Molex pins were provided near the cold end for connections to the tip and sample. Hermetically sealed feedthroughs mounted on blank flanges were fixed at the upper end of the cryostat.

The heating and monitoring wires from the temperature controller were attached to a single 8-pin female connector which could be plugged into a mating connector mounted on the probe. The resistance of a Cernox thin-film temperature sensor mounted on the sample holder using GE-Varnish is monitored using a pseudo-fourprobe configuration requiring two twisted pair cables for the excitation current, and voltage drop measurement. Cernox sensors have very low dependence on magnetic fields, and experiments have determined an error margin of 2% for temperature measurements in a 13 Tesla magnetic field (Heine and Lang 1998).

A quarter watt metal film resistor was used as the heating element.

The current and voltage probes from the AC/DC current source and the Nanovoltmeter were fed to a distribution box using BNC connectors. From the distribution box, a ten core shielded cable was used to relay the signals to the Point contact Probe. Such a configuration enables switching to a different data acquisition setup if required.

2.3.3 Data acquisition software

The entire software development was carried out using open-source tools, taking care not to introduce proprietary dependencies in the finished product. A Qt based interface was designed using Qt-Designer and Pyside (*Qt Project*), and the python (*Python*) programming language is used to run the code on an Ubuntu platform.

Numerical-Python (*Numerical Python*) is used to carry out array manipulations and calculations, and the *PyQtGraph* (*PyQtGraph.org*) *scientific graphics and GUI library* handles data plotting.

The Instruments directly connected to the acquisition computer are the Keithley current source, the Lakeshore temperature controller, and the Atmega32 based stepper motor controller. The nanovoltmeter is attached to the current source via an RS232 cable and a trigger link, and it can be controlled by addressing the current source.

Since the Current source and temperature controller both have TCP as well as GPIB (<http://linux-gpib.sourceforge.net/>) interfaces, support for both communication channels was implemented.

A separate set of tools was developed in order to normalize the acquired data, as well as plot multiple datasets along with appropriate legends.

The entire source code can be found at <https://github.com/jithinbp/Python-gpib-PCAR>

The procedure for setting up GPIB on Ubuntu can be found on several online sources (Hess 2008; *CL-Cambridge*; B.P. 2009)

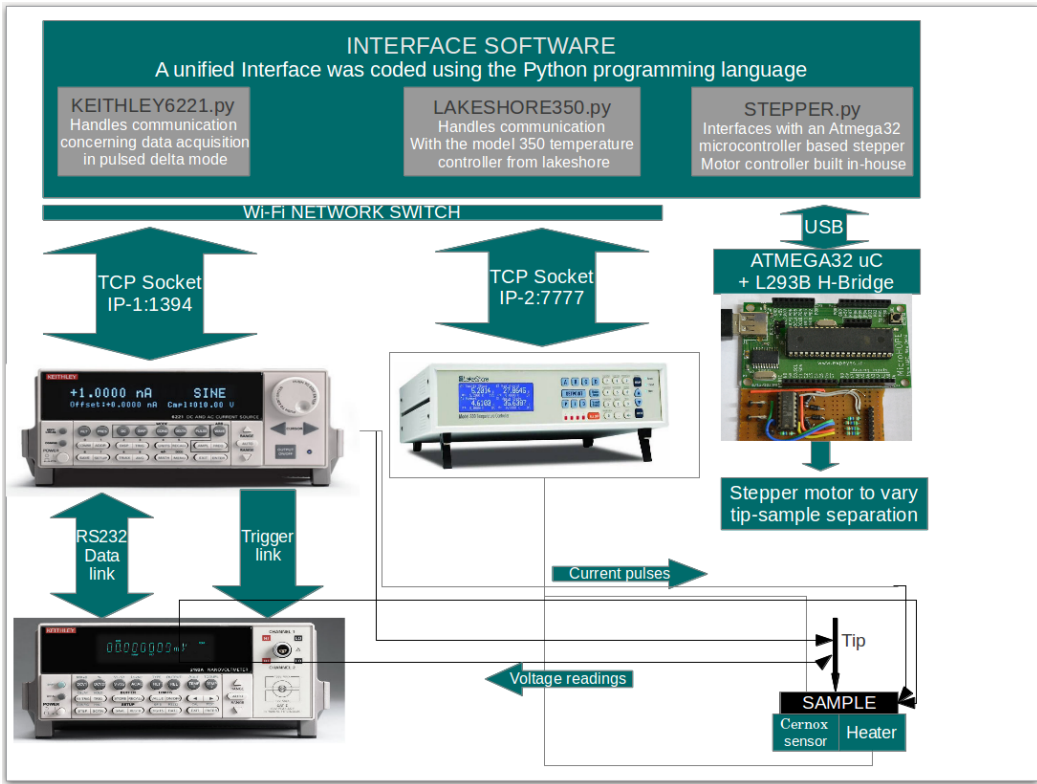


Figure 2.6: Schematic representation of the data acquisition setup

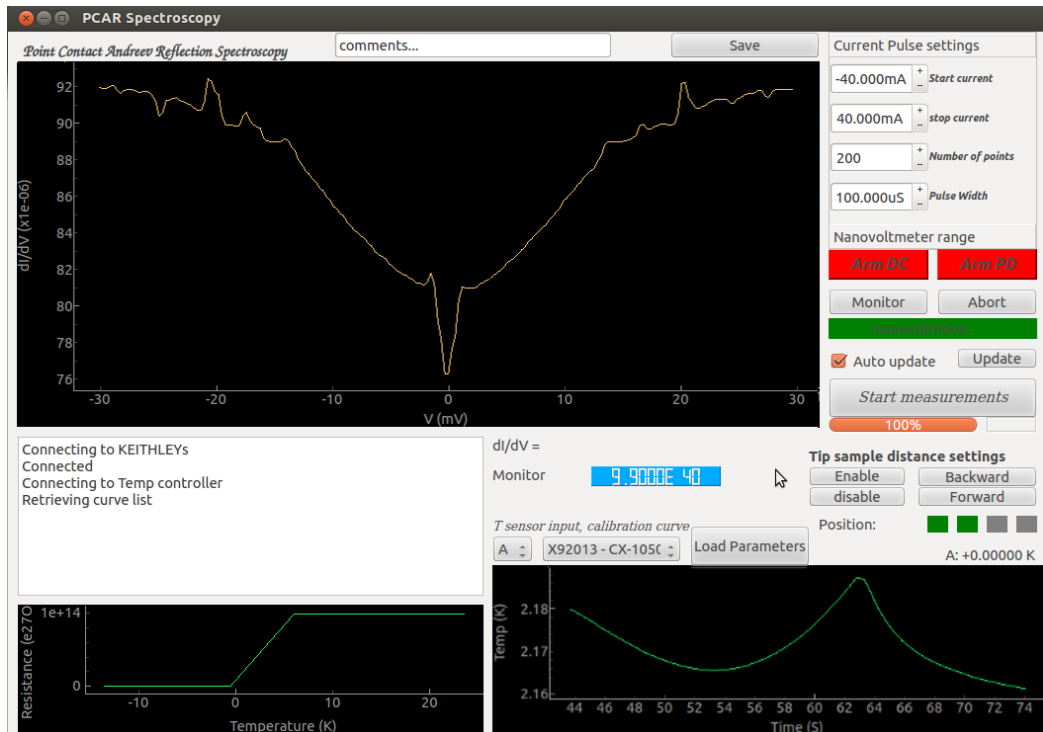


Figure 2.7: Screenshot of open-source software developed to interface with all the instruments.

2.3.4 Acquiring differential resistance data

The Keithley Current source(6221) is connected to a Nanovoltmeter(2182a) via an RS232 cable, and a trigger link, and the two work as a single instrument. All parameters regarding data acquisition are communicated to the current source, and it uses the voltage readings acquired from the triggered NanoVolmeter via RS232 in order to calculate the differential conductance. Nanovoltmeter parameters such as the measurement range can be set by issuing commands to the current source.

The set of commands issued in order to arm differential conductance, and start measurements are as follows

- :syst:comm:ser:send ":sens:volt:rang nanovoltmeter range"
- SOUR:DCON:STARt starting current value for sweeping
- SOUR:DCON:STOP stop current value for sweeping
- SOUR:DCON:STEP step size of the current pulses
- SOUR:DCON:DELTa size of dI
- SOUR:DCON:DELay 1E-1 settling delay for each pulse
- SOUR:SWE:RANG BEST
- :FORM:ELEM AVOL,READ Read datapoints with column 1 as voltage, and column 2 as differential conductance
- SOUR:DCON:ARM Arm differential conductance
- :INIT:IMM start measurements

2.3.5 Acquiring pulsed I-V data

The above mentioned setup can be configured to acquire current-voltage spectra by using independent current pulses. Current pulses can be programmed to have a minimum width of $55\mu S$, and can be swept linearly, as well as logarithmically.

2.3.6 Monitoring temperature

The developed software continuously logs and plots the temperature readings read from the Lakeshore temperature controller. It automatically retrieves all the calibration curves stored within the controller, and allows the user to select the relevant input and curve.

Temperature logging is run in a separate thread in order to obtain uniform datapoints that indicate the rise in sample temperature when it is being measured.

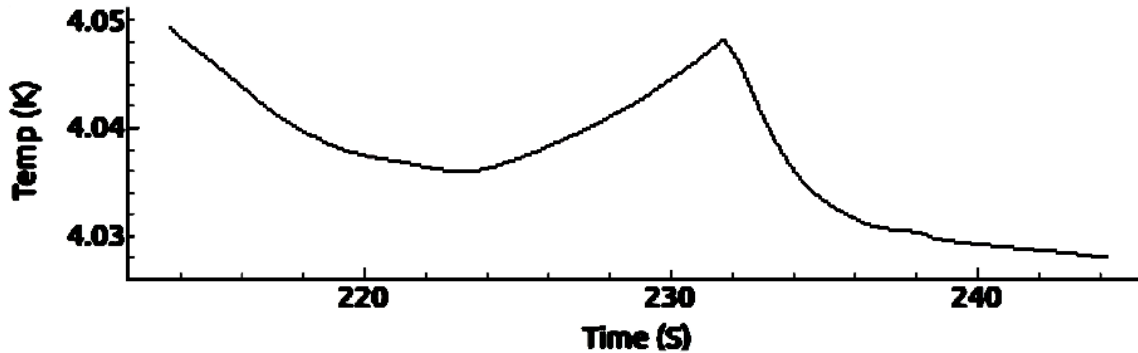


Figure 2.8: Sample temperature rising by about 10mK when measurement current was swept from -15mA to 15mA in differential conductance mode

2.3.7 Stepper motor controller

Firmware for an ATMEGA32 microcontroller was coded in the C language, compiled with the AVR-GCC compiler, and the generated Hex file was uploaded using Avrdude. This IC generates the stepping signals which are amplified using an H-Bridge (L293B) and input to the coils of the stepper motor.

It is capable of running half-step(0.9 degree), as well as full step(1.8 degree) sequences, and can be controlled or queried using commands issued via USB.

The L293B IC is a four channel, push-pull motor driver , and is capable of powering the coils of the four wire stepper motor.

2.4 Results and discussions

2.4.1 Critical current peaks in $FeTe_{0.60}Se_{0.40}$ - Silver point contacts

The dependence of critical current in diffusive contacts formed between an $FeTe_{0.60}Se_{0.40}$ sample and a tip prepared from silver wire on temperature and magnetic fields was studied using the developed probe. The sample was acquired from Prof. G.D. Varma.

The sample has a broad critical temperature owing to possible inhomogeneity, and it is centred at around 14 Kelvin . $FeTe_{0.60}Se_{0.40}$ is a type 2 superconductor, and the critical temperature of its single crystals has been previously reported to be around 14.5K (Vinnikov et al. 2009).

A section of 0.25mm silver wire was cut at an angle using a sharp pair of scissors in order to obtain a pointed tip. It was then mounted into the tip holder to which the $I+$ contact is permanently attached. A gold wire was wrapped around the silver wire and connected to $V+$. Two contacts were made on the sample using silver epoxy in order to connect the $V-$ and $I-$ wires.

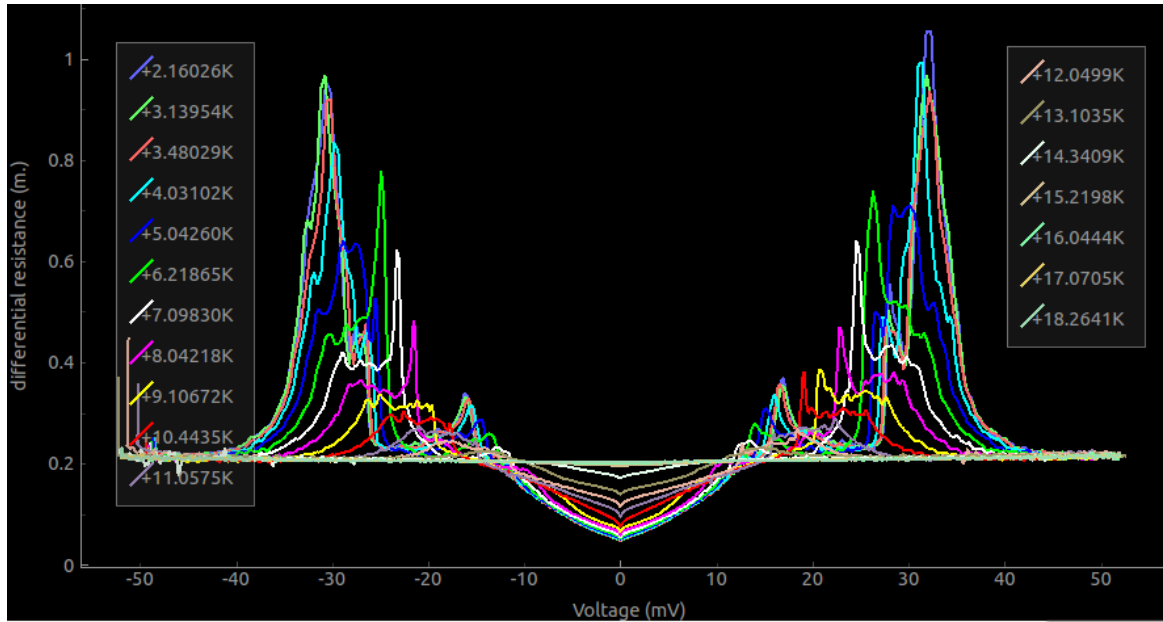


Figure 2.9: Experimental data on temperature dependence of critical current peaks in $FeTe_{0.60}Se_{0.40}$ - Silver point contacts in the thermal regime.

Dependence of critical current on temperature

Superconductivity is broken at a lower value of critical current as the temperature is increased. This occurs due to the added thermal energy which also contributes to breaking up the cooper pair condensate. Higher temperature also causes broadening of the energy distribution in particles, and hence prevents a sharp transition into the resistive state. Eventually, when the temperature reaches the critical limit, superconductivity is broken, and the concept of critical current ceases to exist (Bardeen 1962). The temperature dependence of a $FeTe_{0.60}Se_{0.40}$ -silver point contact was studied over a range of $2K - 18K$, and the results are shown in figure 2.9. Thousand datapoints were acquired for each curve, with a current sweep range of $-100mA$ to $100mA$. dI was set at $100\mu A$.

Dependence of critical current on external magnetic fields

Surface currents are induced in superconductors in response to an external magnetic field. Critical current density is therefore reached for a value of externally injected current that is inversely proportional to the magnetic field applied.

Magnetic fields upto 3 Tesla were applied to a $FeTe_{0.60}Se_{0.40}$ -silver point contact using the PPMS's built in superconducting magnet which was operated in persistent mode. The resultant shifts in the critical current peaks are shown in figure 2.10.

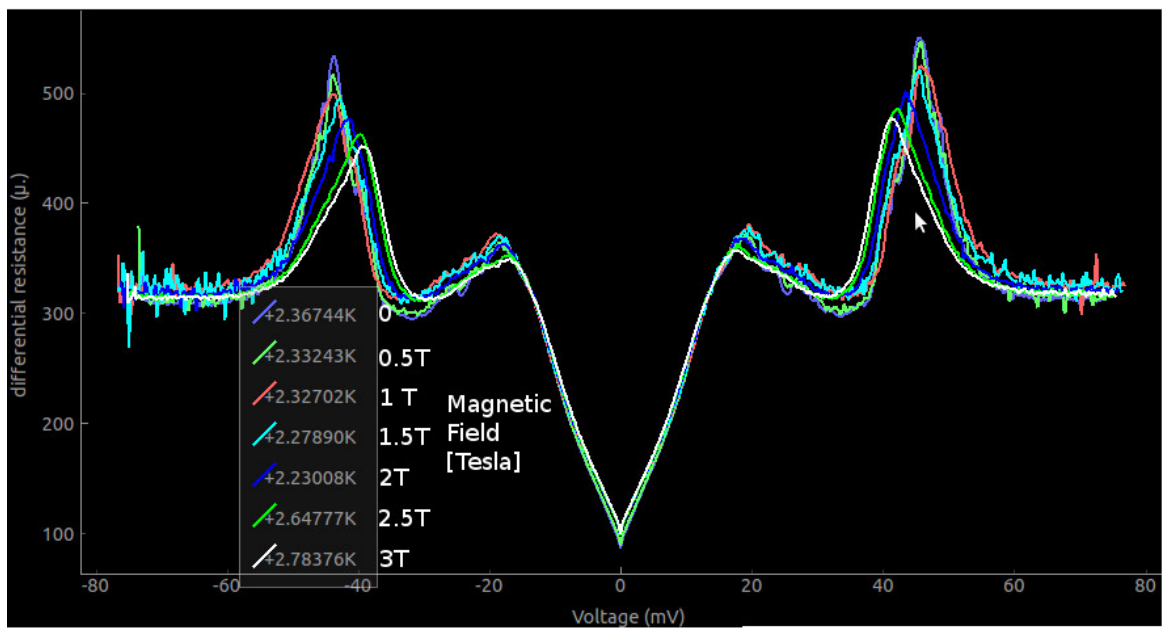


Figure 2.10: Dependence of critical current peaks in $FeTe_{0.60}Se_{0.40}$ - Silver point contacts on external magnetic fields.

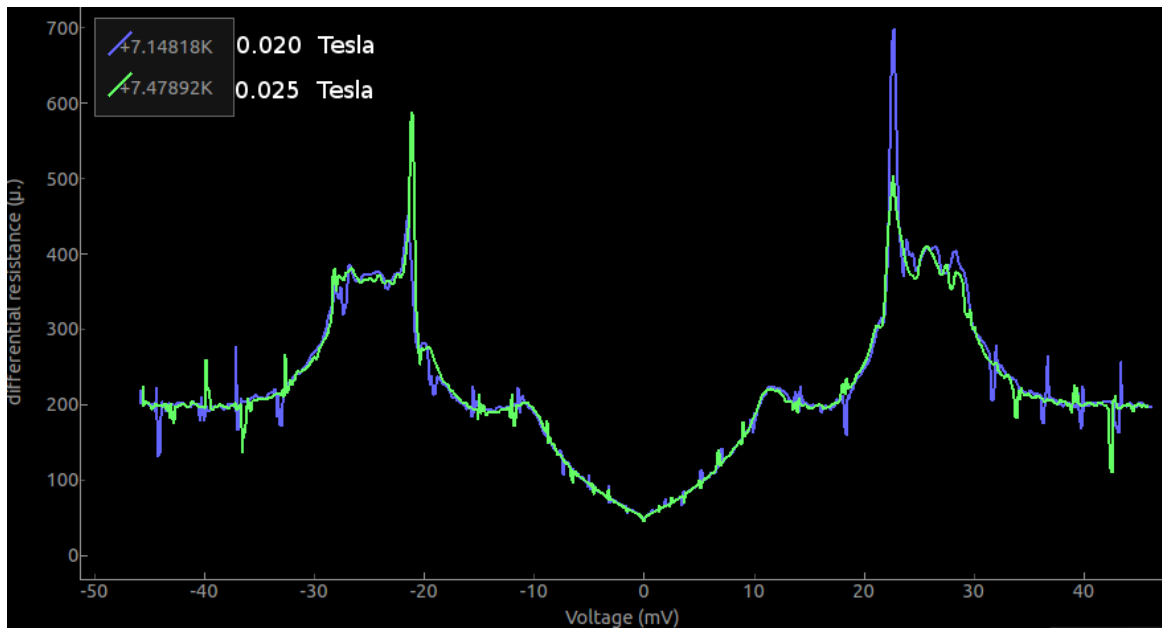


Figure 2.11: Periodic spikes appeared in the differential resistance spectra of $FeTe_{0.60}Se_{0.40}$ -silver point contacts at low magnetic fields from 100 to 300 Oersted. Magnetic field was increased in steps of 50 Oersted from 0 to 300 Oersted.



Figure 2.12: Close up view of the niobium tip facing the gold film. 0.1mm Gold wire contacts on the sample have been mounted using silver epoxy.

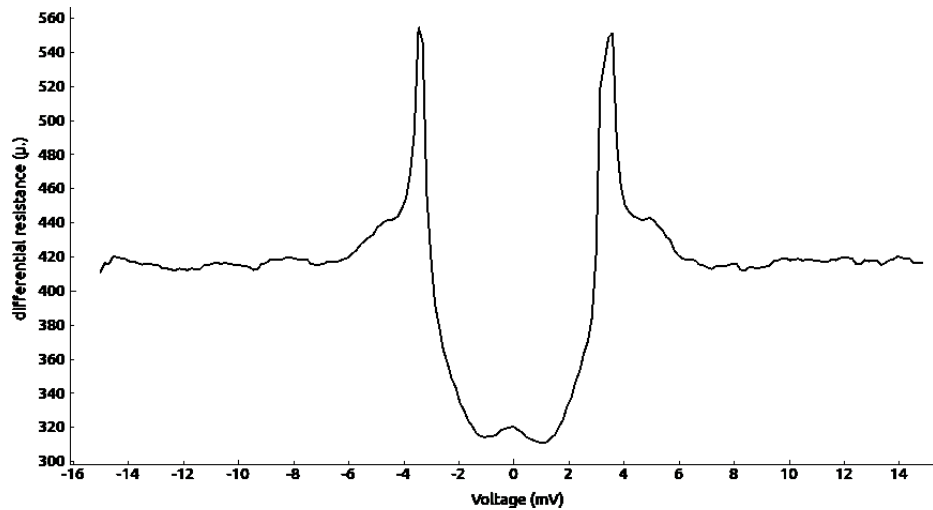


Figure 2.13: PCAR spectra of Niobium-Gold point contact

2.4.2 Andreev reflection spectroscopy in Niobium-Gold contacts

PCAR spectra was obtained for Niobium-Gold point contacts by using a niobium wire as the tip, and a gold thin film as the substrate. The setup is shown in figure 2.12. In order to prepare the sample, DC magnetron sputtering was used to deposit gold on a silicon substrate maintained at 100°C. The normal resistance of the contact was calculated to be $4.15e^{-4}\Omega$ from the differential resistance curve (figure 2.13).

Bibliography

- Assig, Maximilian et al. (2013). “A 10 mK scanning tunneling microscope operating in ultra high vacuum and high magnetic fields.” In: *The Review of scientific instruments* 84.3, p. 033903. URL: <http://www.ncbi.nlm.nih.gov/pubmed/23556826>.
- Bardeen, John (1962). *Critical Fields and Currents in Superconductors*. DOI: [10.1103/RevModPhys.34.667](https://doi.org/10.1103/RevModPhys.34.667).
- Bhatia, Dinesh (1996). *Field-Programmable Gate Arrays*. DOI: [10.1155/1996/87608](https://doi.org/10.1155/1996/87608).
- Binnig, G et al. (1982). “Surface studies by scanning tunneling microscopy”. In: *Physical review letters* 49.1, pp. 57–61. URL: <http://link.aps.org/doi/10.1103/PhysRevLett.49.57>.
- Blonder, G., M. Tinkham, and T. Klapwijk (1982). *Transition from metallic to tunneling regimes in superconducting microconstrictions: Excess current, charge imbalance, and supercurrent conversion*.
- B.P., Jithin (2009). *Virtualization of GPIB instruments on Debian*. Tech. rep. URL: <http://www.scribd.com/doc/33773299/VIRTUALISATION-OF-GPIB-INSTRUMENTS-USING-MODPYTHON-AND-APACHE-WEB-SERVER-ON-DEBIAN-GNU-Linux>.
- Chen, C Julian (2008). *Introduction to scanning tunneling microscopy*. URL: <http://dx.doi.org/10.1093/acprof:oso/9780199211500.001.0001>.
- Choudary, Omar. *CL-Cambridge*. URL: http://www.cl.cam.ac.uk/~osc22/tutorials/gpib_usb_linux.html.
- Daub, Shannon J (2010). “Scanning Tunneling Microscopy : Principle and Instrumentation”. In: *Symbolic Interaction* 33.1, pp. 115–140.
- design, Quantum. *Physical property measurement system(PPMS)*. URL: <http://www.qdusa.com/products/ppms.html>.
- Erts, D. et al. (2000). “Maxwell and Sharvin conductance in gold point contacts investigated using TEM-STM”. In: *Physical Review B* 61.19, pp. 12725–12727. URL: http://prb.aps.org/abstract/PRB/v61/i19/p12725_1.
- Heine, G and W Lang (1998). *Magnetoresistance of the new ceramic Al_2O_3 thermometer from 4.2K to 300K in magnetic fields up to 13T*. DOI: [10.1016/S0011-2275\(97\)00130-6](https://doi.org/10.1016/S0011-2275(97)00130-6).

- Hess, Frank Mori (2008). *Linux Gpib*. URL: http://linux-gpib.sourceforge.net/doc_html/index.html.
- Jansen, A G M, Gelder, and Wyder (1980). “Point-Contact Spectroscopy in Metals”. In: *J. Phys. C: Solid St. Phys.* 13, pp. 6073–6118. ISSN: 0031-8949. DOI: [10.1088/0022-3719/13/33/009](https://doi.org/10.1088/0022-3719/13/33/009). URL: (<http://iopscience.iop.org/0022-3719/13/33/009>.
- Janson, Lucas et al. (Oct. 2012). “Undergraduate experiment in superconductor point-contact spectroscopy with a Nb/Au junction”. In: *American Journal of Physics* 80.2, p. 133. arXiv:[1110.6254](https://arxiv.org/abs/1110.6254). URL: <http://arxiv.org/abs/1110.6254>.
- Keithley. “Low-Level Pulsed Electrical Characterization with the Model 6221 / 2182A Combination”. In: 2611.
- Lee, Chengkuo et al. (1997). “Characterization of micromachined piezoelectric PZT force sensors for dynamic scanning force microscopy”. In: *Review of Scientific Instruments* 68.5, p. 2091. URL: <http://link.aip.org/link/RSINAK/v68/i5/p2091/s1&Agg=doi>.
- Nikolic, Branislav and Philip B Allen (1998). “Electron transport through a circular constriction”. In: *Arxiv.org*, pp. 1–9. arXiv:[9811296v1 \[arXiv:cond-mat\]](https://arxiv.org/abs/9811296v1).
- Numpy.org. *Numerical Python*. URL: [Numpy.org](https://numpy.org).
- Okano, M. et al. (1987). “Vibration isolation for scanning tunneling microscopy”. In: *Journal of Vacuum Science & Technology A: Vacuum, Surfaces, and Films* 5.6, pp. 3313–3320. ISSN: 07342101. DOI: [10.1116/1.574189](https://doi.org/10.1116/1.574189). URL: <http://link.aip.org/link/?JVA/5/3313/1>.
- PI Piezo ceramics. “Pt120 - pt140”. In: pp. 26–27.
- Probst, Oliver M. (2002). *Tunneling through arbitrary potential barriers and the apparent barrier height*.
- Pyside. *Qt Project*. URL: <https://qt-project.org/wiki/PySide>.
- Python.org. *Python*. URL: python.org.
- Redinger W. A. Hofer, J. (1998). *Electronic structure of a realistic STM tip: the role of different apex atoms*. DOI: [10.1080/014186398257790](https://doi.org/10.1080/014186398257790).
- research, Asylum. “3D Calibration Reference”. In: Figure 3.
- Simson, M B (1987). “Signal averaging.” In: *Circulation* 75.4 Pt 2, pp. III69–I78.
- systems, Attocube (2010). “http://www.rockgateco.com/documents/attocube/Brochure_nanoPOSITIONING.pdf”. In:
- Taylor, M. E. (1993). “Dynamics of piezoelectric tube scanners for scanning probe microscopy”. In: *Review of Scientific Instruments* 64.1, p. 154. ISSN: 00346748. DOI: [10.1063/1.1144418](https://doi.org/10.1063/1.1144418). URL: <http://scitation.aip.org/content/aip/journal/rsi/64/1/10.1063/1.1144418>.
- Topinka, M. A. (2000). *Imaging Coherent Electron Flow from a Quantum Point Contact*. DOI: [10.1126/science.289.5488.2323](https://doi.org/10.1126/science.289.5488.2323).

- Vieira, S. (1986). *The behavior and calibration of some piezoelectric ceramics used in the STM*. DOI: [10.1147/rd.305.0553](https://doi.org/10.1147/rd.305.0553).
- Vinnikov, L. Ya. et al. (2009). “Vortex structure in superconducting iron pnictide single crystals”. In: *JETP Letters* 90.4, pp. 299–302. ISSN: 0021-3640. DOI: [10.1134/S0021364009160152](https://doi.org/10.1134/S0021364009160152). URL: <http://link.springer.com/10.1134/S0021364009160152>.
- Wexler, G. (1966). “No Title”. In: *Proc. Phys. Soc. London* 89.927.